Monte Carlo simulations of the diffuse backscattering Mueller matrix for highly scattering media

Sebastian Bartel and Andreas H. Hielscher

We have developed a Monte Carlo algorithm that computes all two-dimensional elements of the diffuse backscattering Mueller matrix for highly scattering media. Using the Stokes–Mueller formalism and scattering amplitudes calculated with Mie theory, we are able to consider polarization-dependent photon propagation in highly scattering media, including linearly and circularly polarized light. The numerically determined matrix elements are compared with experimental data for different particle sizes and show good agreement in both azimuthal and radial direction. © 2000 Optical Society of America

OCIS codes: 260.5430, 170.5280, 290.1350, 290.4210, 290.7050, 290.4020.

1. Introduction

In recent years there has been an increasing interest in the propagation of polarized light in randomly scattering media, especially for medical applications. For example, Schmitt *et al.*,[1] Emile *et al.*,[2] and Demos and Alfano[3] proposed use of polarized light to isolate ballistic photons from the diffuse background and enhance the spatial resolution in optical tomographic methods. In other applications that are aimed at the *in vivo* characterization of biological tissue, the investigation of backscattered light is of particular interest. Anderson,[4] Jacques *et al.*,[5] and Demos and Alfano[6] investigated the utilization of backscattered polarized light for beneath-the-surface imaging. Several studies suggest that relevant information can be obtained from measurements of the spatially dependent response of a medium to a polarized point source.[7–9] In this case a linearly polarized, collimated laser beam is focused to a small point on the medium, and the multiply scattered, diffusely backreflected light around this point is recorded with a CCD camera. Using a collinear or crossed analyzer in front of the camera, one obtains two-dimensional, polarization-dependent, surface intensity maps, which show characteristic two- or fourfold symmetries. It has been demonstrated that these patterns can be used to determine the scattering coefficient μ_s, the anisotropy factor g, and the average size of particles in polystyrene sphere and biological cell suspensions.[8]

Beyond obtaining surface intensity maps of linearly polarized light with crossed or collinear source detector arrangements, many other configurations are possible. For example, one may vary the angle between the optical axes of the linear polarizer and analyzer, or include circularly polarized light into the measurements. It has been shown that a total of 16 intensity measurements suffice to obtain the so-called Mueller matrix, which can be used to describe any optical system.[10–13] This 4×4 matrix operator completely determines the transformation of an arbitrary incident polarization state. In the case of diffusely backscattered light generated by point illumination, each matrix element is represented by a two-dimensional surface map.[14] In previous studies, our group showed that suspensions of differently sized particles show distinctively different backscattering Mueller matrices. Moreover, we were able to differentiate cancerous from noncancerous cell suspensions.[8,14]

In addition to experimental studies, several groups have developed analytical and numerical models that describe polarized light propagation in scattering media. Voshchinnikov and Karjukin[15] investigated the polarized radiation transfer through circumstellar dust shells. Chuah and Tan[16] studied the radar backscatter from random media. Both groups used Monte Carlo algorithms that were based on the Stokes–Mueller formalism. However, none of these groups actually determined elements of the diffuse

The authors are with the Department of Pathology, Box 25, State University of New York, Downstate Medical Center, 450 Clarkson Avenue, Brooklyn, New York 11203. A. H. Hielscher's e-mail address is ahielscher@netmail.hscbklyn.edu.

Received 14 June 1999; revised manuscript received 29 November 1999.

0003-6935/00/101580-09$15.00/0

backscattering Mueller matrix of the medium, nor did they calculate the two-dimensional surface patterns that are observed when linearly polarized light is used.

Dogariu and Asakaru[17] showed that the fundamental fourfold symmetry in the linear degree of polarization of diffusely backscattered light can be explained by assuming photon trajectories with only two scattering events. Kattawar *et al.*[9] and Rakovic *et al.*[18] were the first to present a Monte-Carlo-based method to compute the effective backscattering Mueller matrix and compare it with experimental results obtained from the suspension of polystyrene spheres. They were able to reproduce the azimuthal symmetry in all 16 matrix elements for particles of 2020 nm in diameter, but obtained only poor agreement in the radial dependence.

In this paper we extend the existing approaches and simulate polarization-dependent photon propagation through multiply scattering media. Our simulation fully considers both polar- and azimuthal-dependent scattering as described by Mie theory. Unlike Rakovic *et al.*,[18] who estimated the contribution of each scattered photon by an escape function from a particular scattering location, we follow each photon until it is either absorbed or leaves the medium. By propagating the Stokes vector along with each photon, we can trace the polarization state of individual photons and determine the effective backscattering Mueller matrix.

In Section 2 we briefly review the basic concept of Monte Carlo techniques and the Stokes–Mueller formalism. We provide a detailed description of how the Stokes–Mueller formalism is combined with the Monte Carlo technique to properly consider polarization-dependent light scattering and propagation. In Section 3, simulation results for 204-nm-diameter and 2040-nm-diameter sphere suspensions are compared with experimental results.

2. Numerical Model

A. Basic Monte Carlo Techniques

The basis of our Monte Carlo code for polarized light scattering is an algorithm previously developed by Wang and Jacques.[19,20] The individual photon paths are traces from a pencil beam, normally incident on a slab geometry. The transport path length s between scattering events is sampled randomly from the normalized distribution $\rho(s) = \mu_t \exp(-\mu_t s)$, where $\mu_t = \mu_a + \mu_s$ is the interaction coefficient. A variance reduction technique, namely, use of photon packets, is employed to reduce computational expense and to improve statistics for long photon paths. Rather than being completely absorbed, these packets merely drop statistical weight as they travel through the medium. At each scattering point, the loss is given by $\Delta w = \mu_a/(\mu_a + \mu_s)$ to yield an average decay of $\exp(-\mu_a s)$ along the photon's path. Because the weight serves as a multiplicative factor whenever energy is deposited into, or reflected from, the medium, we are effectively simulating many photons along identical paths. Once the weight falls below some threshold, the photon packet is terminated. A more detailed description of Wang *et al.*'s algorithm as well as experimental validation can be found elsewhere.[20–22] Here we concentrate on the adaptation of this code to consider polarized light.

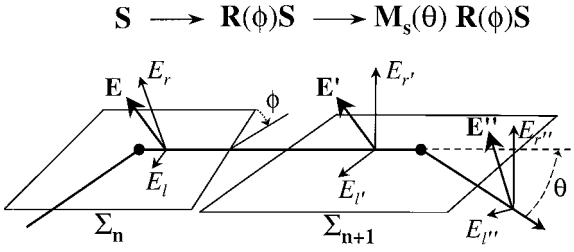

Fig. 1. Transformation of incident Stokes vector **S** into scattering plane by $\mathbf{R}(\phi)$ and subsequent scattering by the single-scattering Mueller matrix $\mathbf{M}_s(\theta)$. Shown are the electric field components, E_1 and E_r, from which the four-Stokes parameters are derived [Eq. (1)].

B. Stokes–Mueller Formalism

To include polarization effect into the standard Wang–Jacques code we employ the Stokes–Mueller formalism of polarized light. The Stokes notation is favored over the also widely used Jones formalism because the latter does not allow for the treatment of depolarizing effects.[10] A detailed discussion of differences and relationships between both approaches can be found in Refs. 10, 23, and 24. Here we only review the basic principles of the Stokes–Mueller formalism. Neglecting only the absolute phase, one can completely describe a given state of polarization in terms of its intensities by a Stokes vector[10,11,25]:

$$\mathbf{S} = \begin{bmatrix} S_0 \\ S_1 \\ S_2 \\ S_3 \end{bmatrix} = \begin{bmatrix} \langle |E_l|^2 + |E_r|^2 \rangle \\ \langle |E_l|^2 - |E_r|^2 \rangle \\ \langle E_l^* E_r + E_l E_r^* \rangle \\ i\langle (E_l^* E_r - E_l E_r^*) \rangle \end{bmatrix}, \tag{1}$$

where E_r and E_l are two orthogonal electrical field components in a plane perpendicular to the propagation direction (Fig. 1). The Stokes parameter S_i are ensemble averages (or time averages in case of ergodic, stationary processes) as indicated by the $\langle\ \rangle$. Therefore no coherence effects are considered. The parameters are real and obey the inequality

$$S_0^2 \geq S_1^2 + S_2^2 + S_3^2. \tag{2}$$

In inequality (2) the equality holds for 100 percent polarized light. The degree of polarization Φ is defined by

$$\Phi = \sqrt{S_1^2 + S_2^2 + S_3^2}/S_0. \tag{3}$$

When Stokes vectors are used to describe the propagation of light through optical components such as lenses, polarizers, and retarders, each of these optical elements can be represented uniquely by a 4×4 Mueller matrix **M**. By multiplying the Stokes vector $\mathbf{S}_0$ of the incident polarization state with the appro-

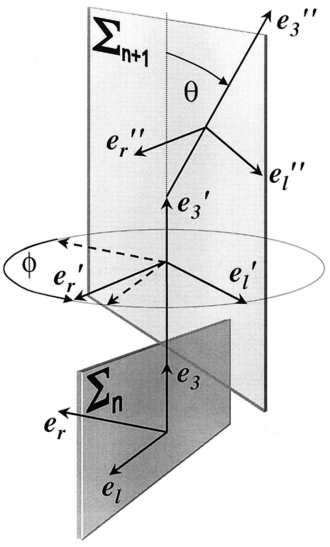

Fig. 2. Local coordinate systems of the photon prior to and after scattering. The photon is incident from below; the scattering plane is denoted Σ_{n+1}.

priate Mueller matrix, one obtains the resulting vector $\mathbf{S}'$ for the transmitted or reflected light. An arrangement of several optical components is described mathematically by successive premultiplication of the corresponding matrix operator:

$$\mathbf{S}' = \mathbf{M}_n \ldots \mathbf{M}_2 \cdot \mathbf{M}_1 \cdot \mathbf{S}_1. \tag{4}$$

C. Polarized Light Propagation in Multiple-Scattering Media

When the Stokes–Mueller formalism is employed to describe scattering events, the Stokes vector $\mathbf{S}$ is defined with respect to the scattering plane Σ, which contains the direction vectors of the ingoing and outgoing beams. E_l is chosen to be in the scattering plane and E_r is orthogonal to the scattering plane (Fig. 1). In multiple-scattering media, this plane of reference changes with each scattering event, so that the Stokes vector $\mathbf{S}_{r,l}$ of a scattered state is, in general, different from $\mathbf{S}_{r',l'}$ the one that is subjected to the next scattering event. To keep track of a photon's polarization state as it undergoes multiple-scattering events, it is assigned the four-component Stokes vector $\mathbf{S}_{r,l}$ and a local coordinate system (e_r, e_1, e_3) in which $\mathbf{S}_{r,l}$ is defined. The local tripod is chosen so that e_3 points in the direction of propagation, and e_l and e_r are oriented parallel and perpendicular to the plane of reference, respectively (Fig. 2). Both $\mathbf{S}$ and (e_r, e_l, e_3) have to be modified upon each scattering event. Knowledge of the reference system is crucial to a correct interpretation of the current Stokes vector.

If we assume that the deflection angles θ and ϕ have already been fixed properly, then the Stokes vector and the local tripod are updated as follows (See Figs. 1 and 2):

(i) First we project the incident Stokes vector (Eq. 1) given in the coordinate system (e_r, e_l, e_3) into the scattering plane. This can always be achieved by a simple rotation of $\mathbf{S}_{rl}$:

$$\mathbf{S}_{r'l'} = \mathbf{R}(\phi) \cdot \mathbf{S}_{rl}, \tag{5}$$

where ϕ is the tilting angle between successive scattering planes and $\mathbf{R}(\phi)$ is given by

$$\mathbf{R}(\phi) = \begin{bmatrix} 1 & 0 & 0 & 0 \\ 0 & \cos(2\phi) & \sin(2\phi) & 0 \\ 0 & -\sin(2\phi) & \cos(2\phi) & 0 \\ 0 & 0 & 0 & 1 \end{bmatrix}. \tag{6}$$

At this point the Stokes vector $\mathbf{S}_{r',l'}$ is given with respect to the system (e_r', e_l', e_3'), in which the single-scattering Mueller matrix $\mathbf{M}_s(\theta)$ is defined. Now we can perform the matrix vector multiplication and obtain the Stokes vector $\mathbf{S}'_{r'',l''}$ of the scattered photon; hence,

$$\mathbf{S}_{r''l''} = \mathbf{M}_s(\theta) \cdot \mathbf{S}_{r'l'} = \mathbf{M}_s(\theta)\mathbf{R}(\phi) \cdot \mathbf{S}_{rl}. \tag{7}$$

Note that the resulting vector $\mathbf{S}_{r''l''}$ is given with respect to the new coordinate system (e_r'', e_l'', e_3'') of the outgoing photon.

(ii) To keep track of the local coordinate system we rotate the local coordinate system (e_r, e_l, e_3) prior to scattering about e_3 and e_r' to obtain the system (e_r'', e_l'', e_3'') of the outgoing photon (Fig. 2). This step involves standard rotational matrices and is performed easily, because we are dealing with the basis vectors in their eigensystem, e.g.,

$$e_r'' = e_r' = D_3(\phi)e_r, \tag{8}$$

$$e_r'' = \begin{bmatrix} \cos(\phi) & -\sin(\phi) & 0 \\ \sin(\phi) & \cos(\phi) & 0 \\ 0 & 0 & 1 \end{bmatrix} \begin{bmatrix} 1 \\ 0 \\ 0 \end{bmatrix} = \begin{bmatrix} \cos(\phi) \\ \sin(\phi) \\ 0 \end{bmatrix}; \tag{9}$$

and similarly

$$e_l'' = \begin{bmatrix} -\cos(\theta)\sin(\phi) \\ \cos(\theta)\cos(\phi) \\ \sin(\theta) \end{bmatrix}, \tag{10}$$

$$e_3'' = \begin{bmatrix} \sin(\theta)\sin(\phi) \\ -\sin(\theta)\cos(\phi) \\ \cos(\theta) \end{bmatrix}, \tag{11}$$

The sense of direction of the above rotations has to be carefully considered. Although the Stokes vector is being expressed in a rotated system, the three basis vectors are being actively rotated, demanding for the transpose matrix, or a negative angle ϕ.

(iii) As it stands, the system (e_r'', e_l'', e_3'') is given with respect to (e_r, e_l, e_3). To be able to determine the Stokes vector in terms of a fixed coordinate system and eventually apply a detector to exiting

photons, (e_r'', e_l'', e_3'') has to be expressed in terms of the global system (x, y, z). For any vector $\mathbf{a}$ given locally, we obtain the x, y, z representation according to

$$\mathbf{a}_{x,y,z} = e_r \cdot a_r + e_l \cdot a_l + e_3 \cdot a_3. \tag{12}$$

So far no concrete single-scattering matrix $\mathbf{M}_s$ has been specified. Mueller matrices for single-scattering particles of arbitrary shape and composition can be derived from Mie theory.[25,26] In this study we considered only isotropically distributed spherical particles, which reduces the Mueller matrix to four independent elements:

$$\mathbf{M}_s(\theta) = \begin{bmatrix} m_{11} & m_{12} & 0 & 0 \\ m_{12} & m_{11} & 0 & 0 \\ 0 & 0 & m_{33} & m_{34} \\ 0 & 0 & -m_{34} & m_{33} \end{bmatrix}. \tag{13}$$

We used a source code by Bohren and Huffman[25] to determine the scattering amplitudes from which the m_{ij} are derived.

D. Sampling of θ and ϕ

Let us now consider the actual sampling of θ and ϕ. Generally, an incident plane wave is scattered over the whole solid angle, resulting in an intensity distribution $I(\theta, \phi)$. Because we are dealing with discrete photon packets and, consequently, discrete deflection angles, it is necessary to either properly sample (θ, ϕ) or to punish certain packets, depending on their new direction.

A straightforward approach to generate a photon density distribution proportional to $I(\theta, \phi)$ would be to sample $\theta \in [0..\pi]$ and $\phi \in [0..2\pi]$ uniformly and modify the photon's weight w after each scattering event, so that

$$w \rightarrow w\rho(\theta, \phi), \tag{14}$$

where $\rho(\theta, \phi) \propto I(\theta, \phi)$ is the normalized intensity distribution. Here, one makes use of the fact that a packet's contribution to the photon density is always proportional to its weight w. However, this method causes many photons to rapidly lose weight by being scattered into less probable directions. Especially in the case of strongly anisotropic scattering, the resulting statistic is increasingly poor for longer paths.

Therefore, the preferred approach is to directly sample (θ, ϕ) so that the probability density ρ of a packet being scattered under these angles is proportional to the expected intensity $I(\theta, \phi) = S_0'(\theta, \phi)$. We obtain ρ in terms of the Stokes components of an incident state by applying Eqs. (6) and (7):

$$\begin{aligned} \rho(\theta, \phi) \propto I(\theta, \phi) = S_0'(\theta, \phi) &= m_{11}(\theta)S_0 \\ &+ m_{12}(\theta)[S_1 \cos(2\phi) + S_2 \sin(2\phi)] \\ &+ m_{12}(\theta)[S_1 \cos(2\phi) + S_2 \sin(2\phi)] \\ &+ m_{13}(\theta)[S_2 \cos(2\phi) - S_1 \sin(2\phi)] \\ &+ m_{14}(\theta)S_3, \end{aligned} \tag{15}$$

where m_{ij} are the elements of the single-scattering Mueller matrix $\mathbf{M}_s$. Note that Eq. (15) introduces an explicit dependence on the incident polarization state, given by the matrix elements m_{12}, m_{13}, and m_{14}, as well as on the azimuth angle ϕ as demanded by Mie theory. This differs from the approach by Kattawar and Rakovic[9,18] who assumed the scattered intensity $I(\theta, \phi)$ to be proportional only to the m_{11} element and therefore independent of ϕ.

The sampling of $I(\theta, \phi)$ according to Eq. (15) from uniformly generated random numbers is performed with the rejection method.[27] First, two angles (θ, ϕ) are randomly chosen and Eq. (15) is evaluated to yield a number $S_0'(\theta, \phi)$ between 0 and 1. Than a third number S_{rand} between 0 and 1 is randomly generated. If $S_{\text{rand}} \leq S_0'(\theta, \phi)$, than the scattering angles for the next scattering event are fixed to (θ, ϕ). If $S_{\text{rand}} > S_0'(\theta, \phi)$, than a new pair of angles and a new value S_{rand} are randomly chosen until $S_{\text{rand}} \leq S_0'(\theta, \phi)$.

E. Photon Detection

The goal of this study is to determine the backscattering Mueller matrix $\mathbf{M} = \{m_{ij}\}$ defined by

$$\mathbf{S}' = \mathbf{M} \cdot \mathbf{S}, \tag{16}$$

which connects any incident Stokes vector $\mathbf{S}$ with the outgoing vector $\mathbf{S}'$ of backscattered light. Although the Mueller matrix for a random distribution of homogeneous spheres is known to have only 7 independent elements,[18] we explicitly recorded all 16 elements. This allowed us to perform consistency checks and verify the validity of our approach.

A total of 16 linear independent intensity measurements with linear and circular polarizers and analyzers in different azimuthal arrangements are required to determine $\mathbf{M}$. Note that except for m_{11} none of the matrix elements is directly accessible by a single measurement. Instead, one has to solve the set of linear equations generated by Eq. 16.[12] A detailed description of how to derive the actual matrix elements from linear combinations of intensity measurements has been given by Bickel and Bailey[13] and Hielscher *et al.*[14]

Because in our simulation we are able to access the Stokes components directly rather than only intensi-

ties, a total of four runs with the orthogonal basis vectors,

$$\mathbf{S}^1 \equiv (1, 0, 0, 0)^T, \quad \mathbf{S}^2 \equiv (1, 1, 0, 0)^T,$$
$$\mathbf{S}^3 \equiv (1, 0, 1, 0)^T, \quad \mathbf{S}^4 \equiv (1, 0, 0, 1)^T, \tag{17}$$

is sufficient to determine all elements of the backscattering Mueller matrix with only minor algebraic effort. Consider an incident unpolarized photon in state S^2 is launched into the medium. Upon it exiting from the medium, we record its Stokes components in the auxiliary matrix $\hat{m}_i^j$:

$$\hat{m}_i^{\,2} = S_i^{2'} \tag{18}$$

where the superscript $j = 1...4$ indicates one of the incident vectors in Eq. (17) and the subscript $i = 1...4$ refers to the component of the detected vector $\mathbf{S}'$.

In general, if the incident polarization state is $\mathbf{S}^j$, the resulting Stokes vector is added to the jth column of $\hat{m}_i^j$. Because Stokes vectors are additive, they may simply be summed up to yield the average answer of the medium. Finally, the average contribution of an incident state $\mathbf{S}^j$ to the ith component of a recorded Stokes vector $\mathbf{S}'$ is contained in $\hat{m}_i^j$.

It is now straightforward to determine the actual backscattering Mueller matrix $\mathbf{M} = \{m_{ij}\}$. For example, for the incident vector $\mathbf{S}^1$ we obtain per definition

$$(\hat{m}_1^{\,1}, \hat{m}_2^{\,1}, \hat{m}_3^{\,1}, \hat{m}_4^{\,1})^T = \mathbf{S}^{1'} = \mathbf{M} \cdot \mathbf{S}^1 \equiv (m_{11}, m_{21}, m_{31}, m_{41})^T, \tag{19a}$$

from which we directly obtain $m_{i1} = \hat{m}_i^{\,1}$. Similarly one obtains for incident Stokes vectors $\mathbf{S}^2$, $\mathbf{S}^3$, and $\mathbf{S}^4$

$$(\hat{m}_1^{\,2}, \hat{m}_2^{\,2}, \hat{m}_3^{\,2}, \hat{m}_4^{\,2})^T = \mathbf{S}^{2'} = \mathbf{M} \cdot \mathbf{S}^2 \equiv (m_{11} + m_{12}, m_{21} + m_{22}, m_{31} + m_{32}, m_{41} + m_{42})^T, \tag{19b}$$

$$(\hat{m}_1^{\,3}, \hat{m}_2^{\,3}, \hat{m}_3^{\,3}, \hat{m}_4^{\,3})^T = \mathbf{S}^{3'} = \mathbf{M} \cdot \mathbf{S}^3 \equiv (m_{11} + m_{13}, m_{21} + m_{23}, m_{31} + m_{33}, m_{41} + m_{43})^T, \tag{19c}$$

$$(\hat{m}_1^{\,4}, \hat{m}_2^{\,4}, \hat{m}_3^{\,4}, \hat{m}_4^{\,4})^T = \mathbf{S}^{4'} = \mathbf{M} \cdot \mathbf{S}^4 \equiv (m_{11} + m_{14}, m_{21} + m_{24}, m_{31} + m_{34}, m_{41} + m_{44})^T. \tag{19d}$$

When we insert the results from Eq. (19a) into Eqs. (19b)–(19d), the remaining elements are easily found.

F. Depolarization

Some remarks are made here concerning the depolarization of light in the photon picture. After a large number n of scattering, all four components of the Stokes vector are effectively mixed and the resultant vector $\mathbf{S}'^{(n)}$ is given in a randomly oriented coordinate system. Extending Eq. (7) to successive scattering of an incident Stokes vector $\mathbf{S}_0$, we can write

$$\mathbf{S}'^{(n)} = \mathbf{M}(\theta_n)\mathbf{R}(\phi_n) \ldots \mathbf{M}(\theta_2)\mathbf{R}(\phi_2) \cdot \mathbf{M}(\theta_1)\mathbf{R}(\phi_1) \cdot \mathbf{S}_0, \tag{20}$$

where θ_n is the ith scattering angle and ϕ_n is the azimuthal angle between scattering planes $(n - 1)$ and n.

It is interesting to note that the matrix product [Eq. (20)] is actually not changing the degree of polarization Φ [Eq. (3)] of individual photons.[25] Any incident state with $\Phi = 1$ will remain 100% polarized as it undergoes multiple-scattering events. Only the nature of polarization will change. However, in Monte Carlo simulations where a large number of independent photons are launched, the observed polarization state is an incoherent superposition of all possible contributions from Eq. (20), which yields

$$\mathbf{S}_{\text{mean}}{}^{(n)} = \sum_i \mathbf{S}_i^{(n)} = \sum_i \mathbf{M}(\theta_{n,i})\mathbf{R}(\phi_{n,i}) \ldots \mathbf{M}(\theta_{2,i})\mathbf{R}(\phi_{2,i}) \cdot \mathbf{M}(\theta_{1,i})\mathbf{R}(\phi_{1,i}) \cdot \mathbf{S}_0, \tag{20}$$

where i indicates the sum over all detected photons. Therefore the effective Stokes vector will generally yield $\Phi < 1$, and we find the medium to be depolarizing.

3. Results

A. Problem Setup

The experimental setup for studying the polarization state of diffuse backscattered light is described in detail elsewhere.[14] Here we restrict the description to the major components. We used a focused He–Ne laser ($\lambda = 543$ nm) whose beam (diameter $d < 500$ μm) is normally incident onto the medium. The emerging light within an area of 4 cm $\times$ 4 cm around the point of incident was projected through an intermediate image plane onto a 14-bit CCD camera. To avoid the strong specular reflection from the surface of the medium and record only multiply scattered light, an optical mask (2 mm in diameter) was placed in the intermediate plane.

The tissue phantom consisted of aqueous monodisperse polystyrene sphere suspensions with particle sizes of 204 and 2040 nm in diameter. The respective concentrations were chosen so that the resulting reduced scattering coefficient μ_s' equaled 1.9 cm^{-1}. For the recording of the backscattering intensity measurements, approximately 30 ml of each suspension was placed in a beaker, which was 4 cm in diameter.

Within the Monte Carlo simulation, particle size, the refractive index of polystyrene, and water and the particle concentration were chosen identical to the experimental values. These parameters, together with the wavelength $\lambda = 543$ nm, of the laser fix the single-scattering matrix $\mathbf{M}_s$. The simulated phantom was a semi-infinite, randomly distributed ensemble of scatterers. To match the experimental geometry, absorption was set to 100% outside the boundaries of the beaker. We implemented the

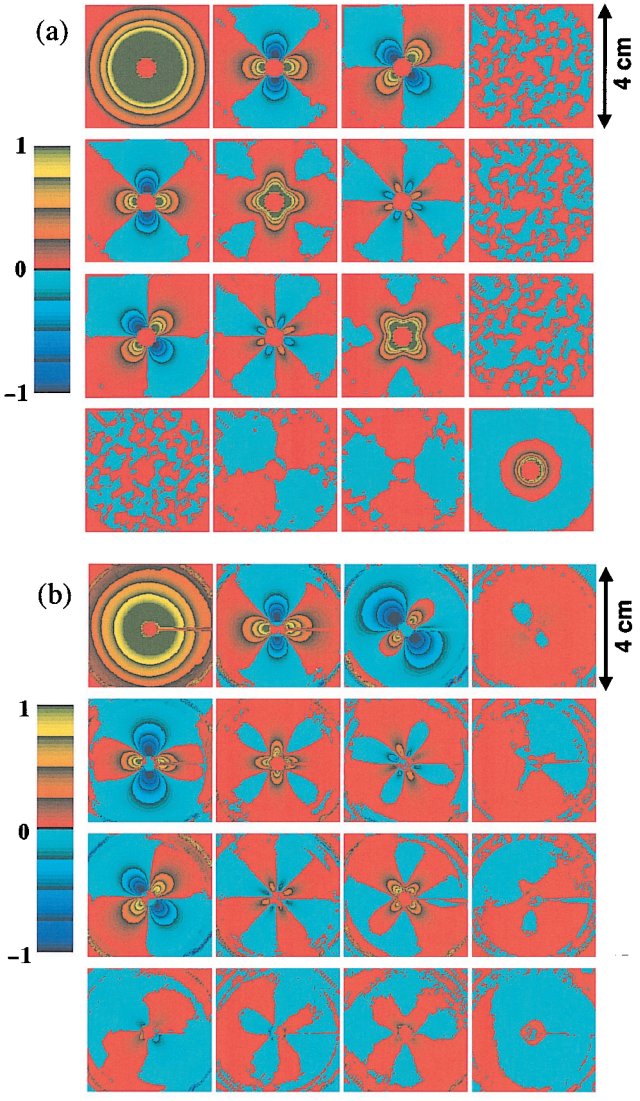

Fig. 3. (a) Simulated backscattering Mueller matrix for the suspension of 204-nm particles. (b) Experimental backscattering Mueller matrix for suspension of 204-nm particles. Each image displays a 4 cm × 4 cm area of the surface.

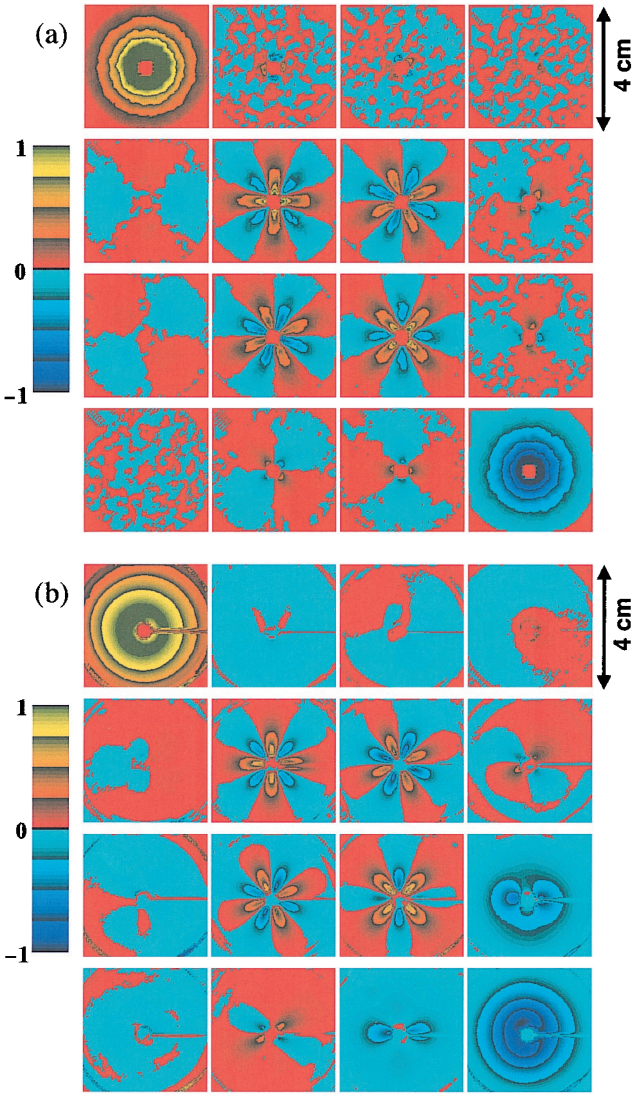

Fig. 4. (a) Simulated backscattering Mueller matrix for suspension of 2040-nm particles. Each image displays a 4 × 4 cm area of the surface. (b) Experimental backscattering Mueller matrix for suspension of 2040-nm particles. Each image displays a 4 cm × 4 cm area of the surface.

Monte Carlo code on a multiprocessor machine, a Cray T3E with 64 Dec Alpha EV 5.6 processors. The total number of photons was divided into equal packages for each processor and these photon packages were processed in parallel. Approximately 2-h computational time was required to propagate 10^8 photons in the suspension that contained 2040-nm-diameter particles. We also employed a cluster of five Linux workstations, each of them with two 450-MHz Pentium processors. On this cluster, simulations with 10^8 photons were completed in less than 16 h. For the 204-nm-diameter-particle suspension, the computation time was reduced by approximately a factor of 5.

B. Comparison of Numerical and Experimental Results

Figures 3 and 4 display the Mueller matrix for suspensions of 204-nm-diameter and 2040-nm-diameter particles, respectively. Each matrix element is given as a two-dimensional image of the surface, 40 × 40 mm in size, with the laser being incident in the center. In the Monte Carlo simulation [Figs. 3(a) and 4(a)], a photon collection grid of 60 × 60 pixels is used, resulting in a spatial resolution of 0.67 mm. This grid size was necessary to improve the signal-to-noise ratio in each pixel. The experimental data [Figs. 3(b) and 4(b)] were obtained with a 300 × 300 grid resulting in a resolution of 0.13 mm. However, to better compare simulations and experiments the experimental data were also projected onto a 60 × 60 grid. All 16 matrix elements are normalized to the maximum intensity of the respective m_{11} element so that the amplitudes range from −1 to +1.

First we note the excellent overall agreement between simulation and experiment. The basic symmetries and structures are recovered for each matrix

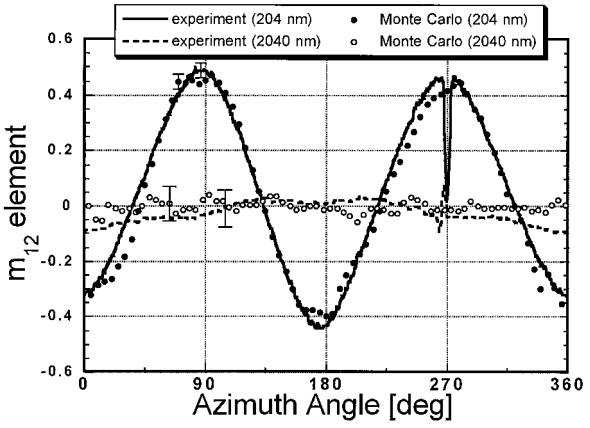

Fig. 5. Comparison of Monte Carlo simulations and experimental results. Shown are values of the m_{12} element on a ring with a 2-cm diameter centered on a light-incident point.

element as well as the backscattering Mueller matrix as a whole. This is true for the azimuthal and radial dependencies for both particles sizes (204-nm sphere and 2040-nm spheres).

As expected, the diffuse reflectance given by element m_{11} is independent of the azimuth. It has a similar radial extent in Figs. 3 and 4 because of the identical μ_s' in all experimental and simulated phantoms. For the 204-nm spheres suspension the last row and column are close to zero, whereas pronounced patterns are observed in columns and rows 1 through 3. The strong lobes in m_{12}, m_{13}, m_{21}, and m_{31} that are characteristic for suspensions of the small polystyrene particles are reproduced accurately in the simulation.

In the case of the 2040-nm spheres suspension, the first row and column are almost zero, except for the m_{11} element. The four central elements have a similar symmetry compared with the small spheres, but show a significantly larger radial extent and higher amplitude. To compare these experimental and theoretical results in more detail, Figs. 5 and 6 show the values of the m_{12} and m_{22} elements along a 2-cm-diameter circle with the center in the middle of the m_{12} and m_{22} images shown in Figs. 3 and 4.

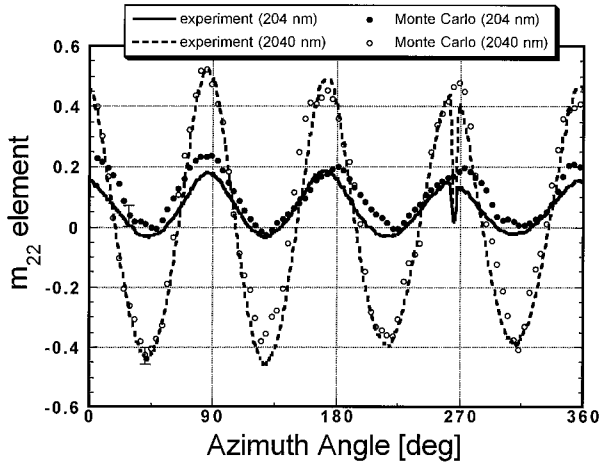

Fig. 6. Comparison of Monte Carlo simulations and experimental results. Shown are values of the m_{22} element on a ring with a 2-cm diameter centered on a light-incident point.

Other differences between the two particle sizes were discussed above,[14] especially the pronounced differences in the m_{44} element, which is close to zero for 204-nm spheres suspension and of the same structure but opposite sign as the m_{11} element for 2040-nm particles suspension. Again, this feature, which was first observed experimentally, is reproduced by the simulations.

4. Discussion

Although good overall agreement with the experiment is observed, some small differences remain. One reason for discrepancies is the uncertainty as to the exact optical parameters, especially the reduced scattering coefficient μ_s'. Because the typical unit length in the diffusion regime is given by $\mu_s'^{-1}$, we can expect the patterns to scale radially with this parameter. For example, regarding the simulated element m_{44} for the 204-nm spheres suspension, we observe a sharp peak in the center. It is almost hidden by the optical mask and is completely invisible in the experiment. However, if we choose a scattering coefficient slightly larger than 1.9 cm^{-1}, the radial extent of the patterns decreases and the positive peaks are covered by the optical mask.

Another potential source of error is the experimental setup. Optical distortions that are due to spherical aberrations, astigmatism, coma, etc., may degrade the image of the surface and slightly change the polarization. These effects will be most notable in elements that are almost zero. The residual azimuthal variation observed in m_{42}, m_{43}, m_{24}, and m_{34} of the experimental data for the 2040-nm sphere suspension may be explained in this way.

Small differences between experiments and simulations may be caused by the fact that the simulations neglect numerical aperture effects. Experimentally, we map the intensity at the surface onto the CCD camera using a setup of lenses with a small aperture. Therefore light escaping normally from the medium is strongly favored over obliquely reflected light. The simulation does consider that the detector can read only electromagnetic oscillations in the x, y plane but integrates over all photons independent of their final direction to provide a reasonable signal-to-noise ratio for each pixel.

Finally, Monte Carlo methods may not be appropriate to describe all polarization effects. Monte Carlo techniques assume that light consists of single photons and that scattering events are independent of each other. No particle–particle interactions are considered. To take these effects into account it may be necessary to directly solve the Maxwell equations for multiple-scattering media—a task that currently appears unapproachable, even with the ongoing advances in computer technology. And, as our results show, basic features of the backscattering Mueller matrix may well be studied and understood with the

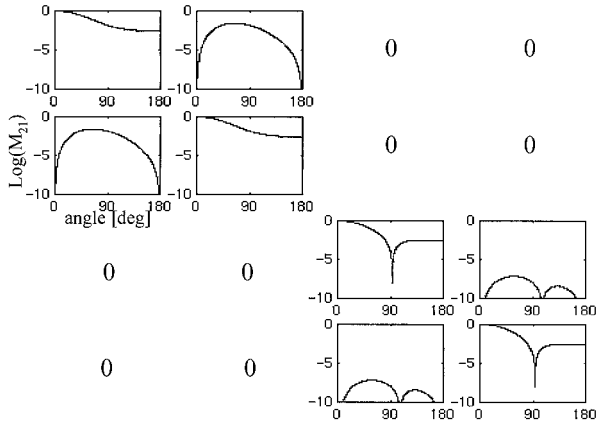

Fig. 7. Nonzero elements of the single-scattering Mueller matrix $\mathbf{M}_{204}$ for a 204-nm-diameter polystyrene sphere at a wavelength of $\lambda = 543$ nm. The log of each matrix element is given as a function of the scattering angle θ.

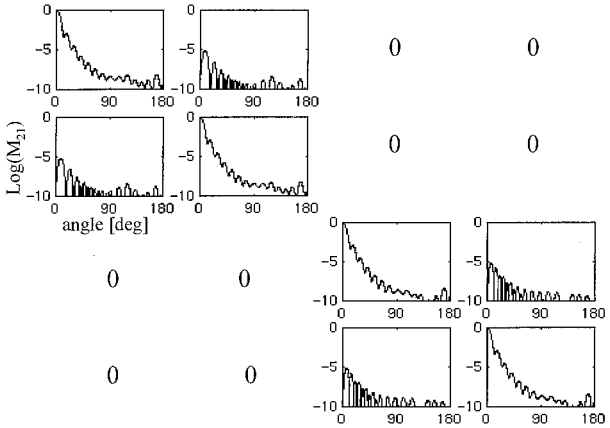

Fig. 8. Nonzero elements of the single-scattering Mueller matrix $\mathbf{M}_{2040}$ for a 2040-nm-diameter polystyrene sphere at a wavelength of $\lambda = 543$ nm.

independent single-scattering event Monte Carlo approach.

Several aspects of the diffusely backscattering Mueller matrix can be deducted when the Mueller matrix for a single-scattering event is considered. The first-row elements m_{12}, m_{13}, and m_{14} of any scattering matrix $\mathbf{M}$ project the Stokes components S_1, S_2, and S_3 of the incident field into the S_0' element of the resulting Stokes vector. Consequently, significant amplitudes in the m_{12}, m_{13}, and m_{14} elements indicate that the scattered intensity depends on the incident state of polarization. The first-column elements m_{21}, m_{31}, and m_{41}, on the other hand, are responsible for transforming any incident intensity S_0 into the components $\mathbf{S}_1'$, $\mathbf{S}_2'$, and $\mathbf{S}_3'$. Thus significant amplitudes in m_{21}, m_{31}, and m_{41} will generate polarized light ($\Phi > 0$) from unpolarized incident light ($\Phi = 0$).

Looking at the diffusely backscattered Mueller matrices in Figs. 3 and 4 we observe that for the 204-nm sphere suspensions, m_{12}, m_{13}, m_{21}, and m_{31} show a strong azimuthal variation whereas the same elements of the 2040-nm sphere suspensions are close to zero. Therefore 204-nm sphere suspensions will generate polarized light at certain areas of the surface, even when the incident light is unpolarized [$\mathbf{S} = (1, 0, 0, 0)$], whereas 2040-nm sphere suspensions will not build up any polarization.

These effects are readily understood as a consequence of the single-scattering matrix $\mathbf{M}_{204}(\theta)$ for 204-nm particles shown in Fig. 7. Here, each nonzero matrix element is plotted on a logarithmic scale as a function of the scattering angle θ. Several things can be observed. First, the diagonal elements have the largest amplitude for most angles. However, the elements m_{12} and m_{21} have significant amplitudes compared with the other elements, especially at scattering angles of 90°. (Note that this angle is not the azimuthal angle used in the diffuse backscattering matrix.) This structure closely resembles that of a partial linear polarizer and is typical for particles small compared to the wavelength, i.e., in the Raleigh regime. We can see that the effects of the single-scattering matrix are preserved in multiple-scattering suspensions, namely, that in both cases polarized light is generated even for unpolarized incident light.

Suspensions of optically nonactive spheres, large compared to the wavelength, do not display strong amplitudes in m_{21}, m_{31}, m_{12}, and m_{13}. This also may be understood if we consult the single-scattering matrix $\mathbf{M}_{2040}(\theta)$ of the 2040-nm spheres (Fig. 8). Here we observe a strong preference for small angles θ in all matrix elements. Furthermore, $\mathbf{M}_{2040}(\theta)$ is diagonally dominant over the whole range of scattering angles and effectively represents an identity operator, which when applied to an incident Stokes vector preserves the initial state over many scattering events. This single-scattering matrix is not capable of generating polarized light from an incident unpolarized beam, which is reproduced in the diffuse backscattering Mueller matrix.

This qualitative reasoning, which is confirmed by both our simulations and the experimental results, allows us to distinguish suspensions of differently sized particles. Furthermore, note that for both types of particles the matrix elements m_{41} and m_{14} are zero. Because optically nonactive spheres provide no mechanism to transform unpolarized light into circularly polarized light, m_{41} necessarily vanishes. In isotropic particle suspensions, the m_{14} element also vanishes because of the intrinsic radial symmetry of a circular state of polarization, which rules out any azimuthal-dependent scattering.

5. Summary

We have developed a Monte-Carlo-based algorithm that accurately models the single-scattering event according to Mie theory and keeps track of the polarization state of individual photons in multiple-

scattering media. We compared simulations of multiple-scattered light to experiments on 204-nm-diameter and 2040-nm-diameter sphere suspensions. The simulations well reproduce the 16, two-dimensional elements of the diffuse backscattering Mueller matrices. We showed that the diffuse backscattering Mueller matrices display characteristics that correspond to features found in the related single-scattering matrices. The developed algorithm provides a tool to examine the effects of different particle sizes and optical properties on observable backscattering polarization patterns from highly scattering media. This allows for future systematic studies regarding the characterization of biological tissue by its backscattering Mueller matrix.

We thank Klaus Ketelsen, system administrator at the Konrad-Zuse-Zentrum für Informationstechnik (ZIB), Berlin, for his valuable advice in the process of implementing the parallel C code and for providing generous access to the computational resources at the ZIB. This research was supported in part by the Dean's Office of the College of Medicine at the State University of New York (SUNY) Health Sciences Center at Brooklyn.

References

1. J. M. Schmitt, A. H. Gandjbakhche, and R. F. Bonner, "Use of polarized light to discriminate short-path photons in a multiply scattering medium," Appl. Opt. **31,** 6535–6546 (1992).
2. O. Emile, F. Bretenaker, and A. Le Floch, "Rotating polarization imaging in turbid media," Opt. Lett. **21,** 1706–1708 (1996).
3. S. G. Demos and R. R. Alfano, "Temporal gating in highly scattering media by the degree of optical polarization," Opt. Lett. **21,** 161–163 (1996).
4. R. R. Anderson, "Polarized-light examination and photography of the skin," Arch. Dermatol. **127,** 1000–1005 (1991).
5. S. L. Jacques, A. Gutsche, J. Schwartz, L. Wang, and F. K. Tittel, "Video reflectometry to extract optical properties of tissue in-vivo," in *Medical Optical Tomography: Functional Imaging and Monitoring*, G. Mueller, B. Chance, R. R. Alfano, S. R. Arridge, J. Beuthan, E. Gratton, M. Kaschke, B. R. Masters, S. Svanberg, and P. van der Zee, eds., Vol. ISII of SPIE Institute Series (SPIE, Bellingham, Wash., 1992), pp. 211–226.
6. S. G. Demos and R. R. Alfano, "Optical polarization imaging," Appl. Opt. **36,** 150–155 (1997).
7. S. L. Jacques, L. H. Wang, D. V. Stephens, and M. Ostermeyer, "Polarized light transmission through skin using video reflectometry: toward optical tomography of superficial tissue layers," in *Lasers in Surgery: Advanced Characterization, Therapeutics, and Systems VI*, R. R. Anderson, ed., Proc. SPIE **2671,** 199–220 (1996).
8. A. H. Hielscher, J. R. Mourant, and I. J. Bigio, "Influence of particle size and concentration on the diffuse backscattering of polarized light from tissue phantoms and biological cell suspensions," Appl. Opt. **36,** 125–135 (1997).
9. G. M. Kattawar, M. J. Rakovic, and B. D. Cameron, "Laser backscattering polarization patterns from turbid media: theory and experiment," in *Advances in Optical Imaging and Photon Migration*, J. G. Fujimoto and M. S. Patterson, eds., Vol. 21 of OSA Trends in Optics and Photonics Series (Optical Society of America, Washington, D.C., 1998), pp. 105–110.
10. C. Brosseau, *Fundamentals of Polarized Light* (Wiley, New York, 1998).
11. E. Collett, *Polarized Light: Fundamentals and Applications* (Marcel Dekker, New York, 1993).
12. R. M. A. Azzam, "Mueller-matrix ellipsometry: a review," in *Polarization: Measurement, Analysis, and Remote Sensing*, D. H. Goldstein and R. A. Chipman, eds., Proc. SPIE **3121,** 396–399 (1997).
13. W. S. Bickel and W. M. Bailey, "Stokes vectors, Mueller matrices, and polarized light scattering," Am. J. Phys. **53,** 468–478 (1985).
14. A. H. Hielscher, A. A. Eick, J. R. Mourant, D. Shen, J. P. Freyer, and I. J. Bigio, "Diffuse backscattering Mueller matrices for highly scattering media," Opt. Exp. **1,** 441–454 (1997); http://epubs.osa.org/oearchive/pdf/2826.pdf.
15. N. V. Voshchinnikov and V. V. Karjukin, "Multiple scattering of polarized radiation in circumstellar dust shells," Astron. Astrophys. **288,** 883–896 (1994).
16. H. T. Chuah and H. S. Tan, "A Monte Carlo backscatter model for radar backscatter from a half-space random medium," IEEE Trans. Geosci. Remote Sens. **27,** 86–93 (1998).
17. M. Dogariu and T. Asakaru, "Polarization dependent backscattering patterns from weakly scattering media," J. Opt. (Paris) **24,** 271–278 (1993).
18. M. J. Rakovic, G. W. Kattawar, M. Mehrübeoglu, B. D. Cameron, L. V. Wang, S. Rastegar, and G. L. Cote, "Light backscattering polarization patterns from turbid media: theory and experiments," Appl. Opt. **38,** 3399–3408 (1999).
19. L. H. Wang and S. L. Jacques, "Optimized radial and angular positions in Monte Carlo modeling," Med. Phy. **21,** 1081–1083 (1994).
20. L. H. Wang, and S. L. Jacques, and L. Zheng, "MCML-Monte Carlo modeling of light transport in multilayered tissues," Comput. Methods Programs Biomed. **47,** 131–146 (1995).
21. L. H. Wang and S. L. Jacques, "Monte Carlo modeling of light transport," in *Optical-Thermal Responses of Laser Irradiated Tissue*, A. J. Welch and M. van Gemert (Plenum, New York, 1995), pp. 73–100; (source code available at http://omlc.ogi.edu/software/mc/index.html).
22. A. H. Hielscher, L. Wang, F. K. Tittel, and S. L. Jacques, "Influence of boundary conditions on the accuracy of diffusion theory in time-resolved reflectance spectroscopy of biological tissues," Phys. Med. Biol. **40,** 1957–1975 (1995).
23. R. M. A. Azzam and N. M. Bashara, *Ellipsometry and Polarized Light* (Elsevier North-Holland, New York, 1977).
24. D. G. M. Anderson and R. Barakat, "Necessary and sufficient conditions for a Mueller matrix to be derivable from a Jones matrix," J. Opt. Soc. Am. A **11,** 2305–2319 (1994).
25. C. F. Bohren and D. Huffman, *Absorption and Scattering of Light by Small Particles* (Wiley, New York, 1998).
26. H. C. van de Hulst, *Light Scattering by Small Particles* (Dover, New York, 1981).
27. I. Lux and L. Koblinger, *Monte Carlo Particle Transport Methods: Neutron and Photon Calculations* (CRC Press, Boca Raton, Fla., 1991).